

A high order semi-Lagrangian discontinuous Galerkin method for Vlasov-Poisson simulations without operator splitting

Xiaofeng Cai¹, Wei Guo², Jing-Mei Qiu³

Abstract. In this paper, we develop a high order semi-Lagrangian (SL) discontinuous Galerkin (DG) method for nonlinear Vlasov-Poisson (VP) simulations without operator splitting. In particular, we combine two recently developed novel techniques: one is the high order non-splitting SLDG transport method [Cai, et al., *J Sci Comput*, 2017], and the other is the high order characteristics tracing technique proposed in [Qiu and Russo, *J Sci Comput*, 2017]. The proposed method with up to third order accuracy in both space and time is locally mass conservative, free of splitting error, positivity-preserving, stable and robust for large time stepping size. The SLDG VP solver is applied to classic benchmark test problems such as Landau damping and two-stream instabilities for VP simulations. Efficiency and effectiveness of the proposed scheme is extensively tested. Tremendous CPU savings are shown by comparisons between the proposed SL DG scheme and the classical Runge-Kutta DG method.

Key Words: Semi-Lagrangian; Discontinuous Galerkin; Vlasov-Poisson; Non-splitting; Mass conservative; Positivity-preserving.

¹ Department of Mathematics, University of Delaware, Newark, DE, 19716. E-mail: xfcai89@gmail.com.

² Department of Mathematics and Statistics, Texas Tech University, Lubbock, TX, 79409. E-mail: weimath.guo@ttu.edu. Research is supported by NSF grant NSF-DMS-1620047.

³ Department of Mathematics, University of Delaware, Newark, DE, 19716. E-mail: jingqiu@udel.edu. Research supported by NSF grant NSF-DMS-1522777 and Air Force Office of Scientific Computing FA9550-12-0318.

1 Introduction

This paper focuses on development of a class of high order semi-Lagrangian discontinuous Galerkin (SLDG) methods for Vlasov-Poisson (VP) simulations without operator splitting. This is a continuation of our previous research effort on a high order non-splitting SLDG method for solving linear transport equations [4]. The VP system, arising from plasma applications, is known as a fundamental model for collisionless plasmas with a negligible magnetic field. It reads as follows,

$$\frac{\partial f}{\partial t} + \mathbf{v} \cdot \nabla_{\mathbf{x}} f + \mathbf{E}(\mathbf{x}, t) \cdot \nabla_{\mathbf{v}} f = 0, \quad (1.1)$$

and

$$\mathbf{E}(\mathbf{x}, t) = -\nabla_{\mathbf{x}} \phi(\mathbf{x}, t), \quad -\Delta_{\mathbf{x}} \phi(\mathbf{x}, t) = \rho(\mathbf{x}, t), \quad (1.2)$$

where \mathbf{x} and \mathbf{v} are coordinates in phase space $(\mathbf{x}, \mathbf{v}) \in \mathbb{R}^3 \times \mathbb{R}^3$, \mathbf{E} is the electric field, ϕ is the self-consistent electrostatic potential and $f(t, \mathbf{x}, \mathbf{v})$ is probability distribution function which describes the probability of finding a particle with velocity \mathbf{v} at position \mathbf{x} at time t . The probability distribution function couples to the long range fields via the charge density, $\rho(t, \mathbf{x}) = \int_{\mathbb{R}^3} f(t, \mathbf{x}, \mathbf{v}) d\mathbf{v} - 1$, where we take the limit of uniformly distributed infinitely massive ions in the background. Equations (1.1) and (1.2) have been nondimensionalized so that all physical constants are one.

Particle-in-cell (PIC) methods have long been a standard tool for numerical simulation of the VP system [3]. Such methods are known to be able to generate reasonable results with relatively low computational cost for high-dimensional simulations. A PIC method mainly comprises two components: (a) A collection of N macro-particles are sampled from the initial distribution function, and they are pushed in the Lagrangian framework via solving the characteristic equation

$$\begin{cases} \frac{d\mathbf{x}}{dt} = \mathbf{v}, \\ \frac{d\mathbf{v}}{dt} = \mathbf{E}(\mathbf{x}, t). \end{cases} \quad (1.3)$$

(b) Meanwhile, electric field \mathbf{E} is solved from Poisson's equation (1.2) by means of a mesh-based scheme when needed. Despite of the simplicity of the PIC method, it suffers from the sampling noise of order $\mathcal{O}(1/\sqrt{N})$, which prevents accurate description of physics of interest in many cases. We refer to the classic textbook [3] for a more detailed review of PIC methods. In this work, we

are interested in the SL approach. As with PIC methods, an SL method advances the solution by following characteristics; while, instead of particles, the solution is interpreted based on a fixed mesh, similar to the Eulerian approach. Consequently, such a method is able to conveniently achieve desirable accuracy with the time step restriction only set by the physical quantities such as the plasma frequency, leading to great savings in computational time. Due to the distinguished property, SL approaches have already elicited substantial interest in plasma simulation community [34, 18].

In this paper, we use the widely recognized DG spatial discretization [15] for the VP simulation. The DG method uses a discontinuous approximation space for the numerical solution and test functions, thus being very effective in resolving complex solution structures, such as the filaments arising from phase mixing in the Vlasov simulations. By contrast, a continuous finite element method tends to introduce excessive numerical diffusion by the restrictive continuity requirement of the approximation space, resulting in smears of the solution or spurious oscillations [25]. The Eulerian DG methods in conjunction with the Runge-Kutta (RK) and other time integrators have been applied for the Vlasov model in the literature, see [25, 13, 12, 10, 11]. On the other hand, the major drawback of such Eulerian DG methods is the associated stringent *CFL* condition when an explicit time integrator is employed. The implicit method developed in [10] can avoid the issue, but substantial computational cost would be incurred for solving the resulting nonlinear algebraic equations.

In our previous work, a class of high order SLDG methods has been proposed which incorporates DG spatial discretization into the SL framework with the aim to take advantage of both. To our best knowledge, this is the first non-splitting, locally conservative, and highly accurate (with up to third order accuracy) SLDG scheme in the literature. In this paper, we consider to generalize our scheme to the VP simulations. The first SL method for solving the VP system was developed by Cheng and Knorr in their seminal paper [9], in which an operator splitting strategy was introduced. One prominent advantage of performing operator splitting is that the resulting split equations are linear and in lower dimensions, thus largely simplifying the algorithm design and implementation of SL schemes [18, 7]. Most existing high order SL schemes are designed based on the splitting strategy. In the literature, finite volume based [19], finite difference based [27, 34, 6, 28, 30], and DG based [31, 33] methods are available. However, a splitting error in time will be incurred, which

can be significant and hence compromise accuracy of the numerical solution over long time Vlasov simulations [14]. This observation motivates our study on the development of a non-splitting high order SLDG schemes for the VP system. The SLDG scheme proposed in [32] is based on a flux form and free of splitting error, but still subject to time step restriction, which undermines computational efficiency of the scheme.

When generalizing our non-splitting SLDG transport method to the VP simulation, we need to address an additional difficulty. That is, unlike in the linear transport or the VP simulation with operator splitting setting, the characteristics can no longer be exactly tracked, since their evolution is nonlinear and subject to the electric field that is induced by the unknown function itself. In [29], a novel characteristics tracking strategy with up to third order temporal accuracy is developed via a two-stage multi-derivative prediction-correction approach. We propose in this work to incorporate the strategy to realize high order accuracy in time. It is worthwhile to mention that, in [29], a non-splitting finite difference SL method based on such a characteristics tracking strategy is also proposed, which is high order accurate in both space and time and unconditionally stable, but fails to conserve the total mass. More recently, a mass conservative variant is developed in [37] through a conservative correction technique, yet a time step constraint is introduced for stability.

This paper is organized as follows. In Section 2, we formulate the SLDG scheme for solving the VP system. We also propose an economical version of the SLDG method for computational efficiency. The performance of the proposed method is shown in Section 3 through extensive numerical tests on several benchmark problems for VP simulations. Finally, concluding remarks are made in Section 4.

2 Truly multi-dimensional SLDG algorithm

In this section, we formulate the SLDG method for the VP simulations in two dimensions. We start by introducing the underlying algorithm framework, then the two main components of the proposed SLDG scheme are presented, including a high order characteristics tracing mechanism for the VP system based on a prediction-correction technique as well as the high order SLDG transport scheme. Some implementation details are also provided.

2.1 Algorithm framework

We consider the VP system (1.1) with the one-dimensional (1D) physical space and 1D velocity space on the two-dimensional (2D) domain $\Omega = \Omega_x \times \Omega_v$, where Ω_x is a bounded domain with periodic boundary conditions and $\Omega_v = [-v_{\max}, v_{\max}]$ with v_{\max} chosen large enough so that a zero boundary condition is reasonably imposed. We assume a Cartesian uniform partition of the computational domain $\Omega = \{A_j\}_{j=1}^J$ (see Figure 2.1) for simplicity. In principle, the method can be extended to general unstructured meshes with some modifications in implementation. Such extension will be addressed in our forthcoming paper. We define the finite dimensional piecewise polynomial approximation space, $V_h^k = \{v_h : v_h|_{A_j} \in P^k(A_j)\}$, where $P^k(A_j)$ denotes the set of polynomials of degree at most of k on element A_j . For illustrative purposes, we only present the formulation of the SLDG scheme with P^1 polynomial space. The generalization to P^2 polynomial space follows a similar procedure discussed in [4].

In order to update the solution at time level t^{n+1} over the cell A_j based on the solution at time level t^n , we employ the weak formulation of characteristic Galerkin method proposed in [22, 4]. Specifically, we consider the following adjoint problem for the time dependent test function ψ

$$\psi_t + v\psi_x + E(x, t)\psi_v = 0, \text{ subject to } \psi(t = t^{n+1}) = \Psi(x, v), \quad t \in [t^n, t^{n+1}], \quad (2.1)$$

where $\Psi \in P^k(A_j)$. The scheme formulation takes advantage of the identity

$$\frac{d}{dt} \int_{\tilde{A}_j(t)} f(x, v, t)\psi(x, v, t) dx dv = 0, \quad (2.2)$$

where $\tilde{A}_j(t)$ is a dynamic moving cell, emanating from the Eulerian cell A_j at t^{n+1} backward in time by following characteristics trajectories. The multi-dimensional SLDG scheme is formulated as follows: Given the approximate solution $f^n \in V_h^k$ at time t^n , find $f^{n+1} \in V_h^k$ such that $\forall \Psi \in V_h^k$, we have

$$\int_{A_j} f^{n+1} \Psi(x, v) dx dv = \int_{A_j^*} f^n \psi(x, v, t^n) dx dv, \quad \text{for } j = 1, \dots, J, \quad (2.3)$$

where ψ solves (2.1) and $A_j^* = \tilde{A}_j(t^n)$. A_j^* is called the upstream cell of A_j . In general, A_j^* is no longer a rectangle, for example, see a deformed upstream cell bounded by red curves in Figure 2.1. The proposed SLDG method in updating the numerical solution f^n to f^{n+1} consists of the following two main steps.

1. Construct approximated upstream cells by following characteristics. Denote the four vertices of A_j as c_q , with the coordinates (x_q, v_q) , $q = 1, \dots, 4$ in the phase space. We trace characteristics backward in time to t^n for the four vertices and then obtain c_q^* with the new coordinates (x_q^*, v_q^*) , $q = 1, \dots, 4$. For example, see c_4 and c_4^* in Figure 2.1. Then the upstream cell can be approximated by a quadrilateral determined by the four vertices c_q^* . The new coordinates (x_q^*, v_q^*) of c_q^* are approximated by numerically solving the characteristics equation (2.1) in the 2D case, i.e.,

$$\begin{cases} \frac{dx(t)}{dt} = v(t), \\ \frac{dv(t)}{dt} = E(x(t), t), \end{cases} \quad \text{with} \quad \begin{cases} x(t^{n+1}) = x_q, \\ v(t^{n+1}) = v_q, \end{cases} \quad q = 1, 2, 3, 4, \quad (2.4)$$

which is a set of final value problems. We remark that the above equations are non-trivial to solve with high order temporal accuracy. In particular, note that the electric field E depends on the unknown f via Poisson's equation (1.2) in a global rather than local fashion. To circumvent the difficulty, we propose to combine a high order two-stage multi-derivative prediction-correction strategy for tracing characteristics as proposed in [29]. Such a strategy is briefly described in the context of the proposed SLDG scheme in Section 2.2. If a high order (e.g. third order) approximation is desired, then four sides of A_j^* should be approximated by quadratic curves, in which case more points should be tracked for the curve fitting, see [4] for more details.

2. Update the solution f^{n+1} by evaluating the RHS of eq. (2.3) for $\forall \Psi \in V_h^k$. We approximate A_j^* by a quadrilateral in the previous step. The test function ψ at t^n can be approximated by a polynomial via a least squares procedure by tracking point values of ψ along characteristics. In order to efficiently evaluate the volume integral in the RHS of (2.3), it is converted into a set of line integrals by the use of Green's theorem. Such an idea is borrowed from CSLAM [26], and further reformulated in [4] for the development of an SLDG transport scheme. The above-mentioned procedure is briefly described in Section 2.3.

2.2 High order characteristics tracing prediction-correction algorithm

In this subsection, we describe a high order predictor-corrector procedure for locating the feet of the characteristics of the VP system. Such an approach is originally proposed in [29]. We first introduce several shorthand notations. The superscript n denotes the time level, the superscript (τ)

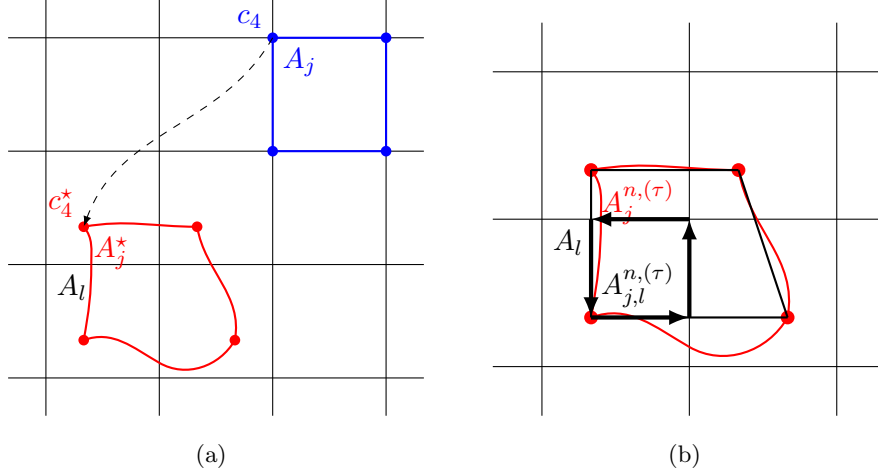


Figure 2.1: Schematic illustration of the SLDG formulation in two dimension: quadrilateral approximation to a upstream cell.

denotes the formal order of approximation for time discretization, and the subscript q is the index for the vertices of the underlying cell in the phase space. For example, $(x_q^{n,(\tau)}, v_q^{n,(\tau)})$ is the τ -th order approximation of (x_q^*, v_q^*) and $A_j^{n,(\tau)}$ is the quadrilateral determined by the corresponding four vertices.

We start from a first order scheme for tracing characteristics (2.4). We let

$$x_q^{n,(1)} = x_q - v_q \Delta t, \quad v_q^{n,(1)} = v_q - E(x_q, t^n) \Delta t, \quad (2.5)$$

which leads to a first order approximations to (x_q^*, v_q^*) . The electric field E depends on f via Poisson's equation, which can be numerically solved by the LDG method [2, 16, 8]. Note that the numerical solution E_h solved by the LDG method are discontinuous across cell boundaries, i.e. $E_h(x_q^+, t^n) \neq E_h(x_q^-, t^n)$, where the superscripts \pm are the right- and left-hand limits of the corresponding functions with respect to x_q . In our implementation, we take the average of E_h at the boundaries as the numerical solution E_q , i.e. $E(x_q, t^n) = \frac{(E_h(x_q^+, t^n) + E_h(x_q^-, t^n))}{2}$. Let $A_j^{n,(1)}$ to be the quadrilateral formed by the four upstream vertices $(x_q^{n,(1)}, v_q^{n,(1)})$, $q = 1, 2, 3, 4$. Then, by the SLDG formulation (to be described in the next subsection)

$$\int_{A_j} f^{n+1,(1)} \Psi(x, v) dx dv = \int_{A_j^{n,(1)}} f^n \psi(x, v, t^n) dx dv, \quad (2.6)$$

we obtain $f^{n+1,(1)}$ as a first order approximation in time to the solution at t^{n+1} . Based on $f^{n+1,(1)}$, we apply the LDG method to Poisson's equation (1.2) again and compute $E_q^{n+1,(1)}$, which approximates $E(x_q, t^{n+1})$ with first order temporal accuracy.

A second order scheme can be built upon the first order one. First, let

$$x_q^{n,(2)} = x_q - \frac{1}{2} (v_q + v_q^{n,(1)}) \Delta t, \quad v_q^{n,(2)} = v_q - \frac{1}{2} (E(x_q^{n,(1)}, t^n) + E_q^{n+1,(1)}) \Delta t, \quad (2.7)$$

which gives a second order approximations to (x_q^*, v_q^*) . Then the second order approximation solution $f^{n+1,(2)}$ is obtained from the SLDG formulation

$$\int_{A_j} f^{n+1,(2)} \Psi(x, v) dx dv = \int_{A_j^{n,(2)}} f^n \psi(x, v, t^n) dx dv. \quad (2.8)$$

Based on $f^{n+1,(2)}$, we are able to compute $E_q^{n+1,(2)}$ from Poisson's equation, which approximates $E(x_q, t^{n+1})$ with second order temporal accuracy.

Lastly, a third order scheme can be designed based on the above second order approximation.

Let

$$x_q^{n,(3)} = x_q - v_q \Delta t + \frac{\Delta t^2}{2} \left(\frac{2}{3} E_q^{n+1,(2)} + \frac{1}{3} E(x_q^{n,(2)}, t^n) \right), \quad (2.9)$$

$$v_q^{n,(3)} = v_q - E_q^{n+1,(2)} \Delta t + \frac{\Delta t^2}{2} \left(\frac{2}{3} \left(\frac{d}{dt} E(x_q, t^{n+1}) \right)^{(2)} + \frac{1}{3} \frac{d}{dt} E(x_q^{n,(2)}, t^n) \right), \quad (2.10)$$

where $\frac{d}{dt}$ is the material derivative along the characteristic curve [29], i.e.,

$$\frac{d}{dt} E = \frac{\partial E}{\partial t} + \frac{\partial E}{\partial x} \frac{\partial x}{\partial t} = \bar{J}^0 - J(x, t) + v(\rho - 1).$$

Note that we have used Ampère's law

$$\frac{\partial E}{\partial t} = \bar{J}^0 - J(x, t),$$

where $J(x, t) = \int f v dv$ is the current density and $\bar{J}^0 = \frac{1}{L} \int J(x, t = 0) dx$ is the average of the current density at $t = 0$ with $L = |\Omega_x|$. In particular, in equation (2.10)

$$\left(\frac{d}{dt} E(x_q, t^{n+1}) \right)^{(2)} = \bar{J}^0 - J_q^{n+1,(2)} + v_q (\rho_q^{n+1,(2)} - 1), \quad (2.11)$$

$$\frac{d}{dt} E(x_q^{n,(2)}, t^n) = \bar{J}^0 - J(x_q^{n,(2)}) + v_q^{n,(2)} (\rho(x_q^{n,(2)}, t^n) - 1). \quad (2.12)$$

It can be checked by a local truncation error analysis that $(x_q^{n,(3)}, v_q^{n,(3)})$ is a third order approximation to (x_q^*, v_q^*) [29]. Consequently, the third order approximation solution $f^{n+1,(2)}$ is updated from the SLDG formulation

$$\int_{A_j} f^{n+1,(2)} \Psi(x, v) dx dv = \int_{A_j^{n,(3)}} f^n \psi(x, v, t^n) dx dv. \quad (2.13)$$

2.3 A two-dimensional SLDG method with quadrilateral upstream cells.

Below, we present the procedure in evaluating the integral $\int_{A_j^*} f^n \psi(x, v, t^n) dx dv$ with a quadrilateral upstream cell A_j^* . In the algorithm design, we have to pay attention to the following two observations, see [4].

- $\Psi = \psi(x, v, t^{n+1})$ is chosen to be polynomial basis functions on V_h^k , while, in general $\psi(x, v, t^n)$ is no longer a polynomial. A polynomial function constructed by a least squares procedure is used to approximate $\psi(x, v, t^n)$.
- Over the upstream cell A_j^* (or its approximation $A_j^{n,(\tau)}$), $f^n(x, v, t^n)$ is discontinuous across Eulerian cell boundaries, see the background Eulerian grid lines in Figure 2.1. To properly evaluate the volume integral, one has to perform the evaluation in a sub-area by sub-area manner. Meanwhile, direct evaluation of volume integrals over these irregular-shape sub-areas is very involved in implementation. The proposed strategy is to convert each volume integral into line integrals by the use of Green's Theorem.

Based on these observations, the proposed algorithm consists of two main components. One is the search algorithm that finds the boundaries for each sub-area, i.e. the overlapping region between the upstream cell and background Eulerian cells. The other is the use of Green's theorem that enables us to convert the volume integral to line integrals based on the result of the search algorithm. Below we describe the detailed procedure in evaluating the volume integral over an approximation of upstream cell $A_j^{n,(\tau)}$ for the SLDG scheme with P^1 polynomial space.

- (1) **Least squares approximation of test function $\psi(x, v, t^n)$.** Based on the fact that the solution of the adjoint problem (2.1) stays unchanged along characteristics, we have

$$\psi(x_q^{n,(\tau)}, v_q^{n,(\tau)}, t^n) = \Psi(x_q, v_q), \quad q = 1, 2, \dots, 4.$$

Thus, we can reconstruct a unique linear function $\psi^*(x, v)$ by a least squares strategy that approximates $\psi(x, v, t^n)$ on $A_j^{n,(\tau)}$.

- (2) **Evaluation of the volume integral.** Denote $A_{j,l}^{n,(\tau)}$ as a non-empty overlapping region between the upstream cell $A_j^{n,(\tau)}$ and the background Eulerian cell A_l , i.e., $A_{j,l}^{n,(\tau)} = A_j^{n,(\tau)} \cap A_l$,

see Figure 2.1 (b). Then the volume integral, e.g. RHS of eq. (2.6) with $\tau = 1$, becomes

$$\int_{A_j^{n,(\tau)}} f(x, v, t^n) \psi(x, v, t^n) dx dv \approx \sum_{l \in \varepsilon_j^{n,(\tau)}} \int_{A_{j,l}^{n,(\tau)}} f(x, v, t^n) \psi^*(x, v) dx dv, \quad (2.14)$$

where $\varepsilon_j^{n,(\tau)} = \{l | A_{j,l}^{n,(\tau)} \neq \emptyset\}$. Note that the integrands on the RHS of (2.14) are piecewise polynomials. By introducing two auxiliary function $P(x, v)$ and $Q(x, v)$ such that

$$-\frac{\partial P}{\partial v} + \frac{\partial Q}{\partial x} = f(x, v, t^n) \psi^*(x, v),$$

the area integral $\int_{A_{j,l}^{n,(\tau)}} f(x, v, t^n) \psi^*(x, v) dx dv$ can be converted into line integrals via Green's theorem, i.e.,

$$\int_{A_{j,l}^{n,(\tau)}} f(x, v, t^n) \psi^*(x, v) dx dv = \oint_{\partial A_{j,l}^{n,(\tau)}} P dx + Q dv, \quad (2.15)$$

see Figure 2.1 (b). Note that the choices of P and Q are not unique, but the value of the line integrals is independent of the choices. In the implementation, we follow the same procedure in [26] when choosing P and Q . In summary, combining (2.14) and (2.15), we have the following

$$\begin{aligned} \int_{A_j^{n,(\tau)}} f(x, v, t_n) \psi(x, v, t_n) dx dv &= \sum_{l \in \varepsilon_j^{n,(\tau)}} \int_{A_{j,l}^{n,(\tau)}} u(x, v, t_n) \psi^*(x, v) dx dv \\ &= \sum_{l \in \varepsilon_j^{n,(\tau)}} \oint_{\partial A_{j,l}^{n,(\tau)}} P dx + Q dv \\ &= \sum_{q=1}^{N_o} \int_{\mathcal{L}_q} [P dx + Q dv] + \sum_{q=1}^{N_i} \int_{\mathcal{S}_q} [P dx + Q dv]. \end{aligned} \quad (2.16)$$

Note that in the above computation, we have organized the liner integrals into two categories: along outer line segments (see Figure 2.2 (b)) and along inner line segments (see Figure 2.2 (c)). Line segments can be uniquely determined by two end points, which are intersection points of the four sides of the upstream cell with grid lines. We compute all intersection points and connect them in a counterclockwise orientation to obtain outer line segments, denoted as \mathcal{L}_q , $q = 1, \dots, N_o$, see Figure 2.2 (b). The line segments that are aligned with grid lines and enclosed by $A_j^{n,(\tau)}$ are defined as inner line segments, see Figure 2.2 (c). Note that there are two orientations along each inner segment, but the corresponding line integrals have to be evaluated in their own sub-area, given that f^n is discontinuous across a inner line segment. For instance, $\overrightarrow{s_1 c_1}$ belongs to the left background cell and $\overleftarrow{c_1 s_1}$ belongs to the right background

cell. Again we refer to [26, 4] for more details in implementation and in generalization to the SLDG scheme with P^2 polynomial space.

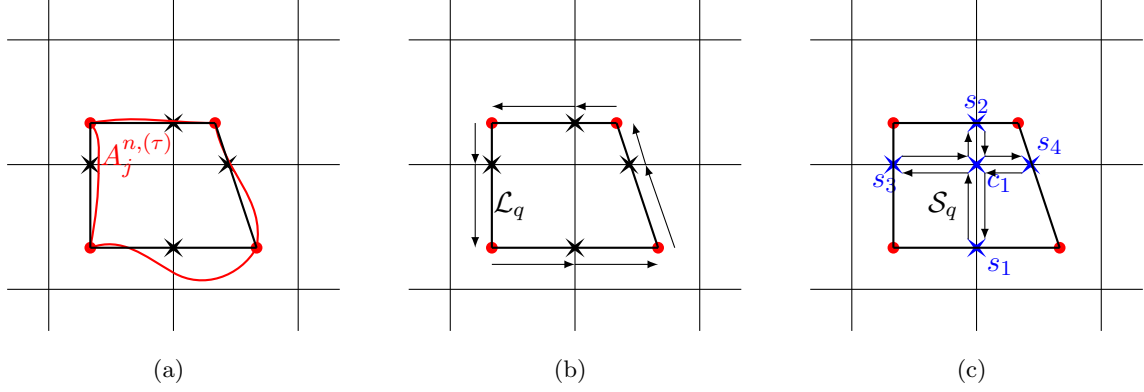


Figure 2.2: Schematic illustration of the search algorithm.

2.4 A two-dimensional SLDG method with quadratic-curved quadrilateral upstream cells.

Note that the aforementioned SLDG methods with quadrilateral approximation yields the second order accuracy even though P^2 approximation space is used. In order to achieve a formal third order accuracy, a quadratic-curved quadrilateral is used to approximate each upstream cell A^* when evaluating of the integral $\int_{A^*} f^n \psi(x, v, t^n) dx dv$. In particular, one can construct a parabola to approximate each side of an upstream cell. Since the procedure of the SLDG scheme with quadratic-curved quadrilateral upstream cells is similar to that of the SLDG scheme with quadrilateral upstream cells, we only highlight the evaluation of line integrals along outer line segments. The procedure of evaluation consists of the following main steps.

(1) *Construction of quadratic-curved upstream cells by following characteristics.*

- (1a) Locate nine points on the upstream cell A_j^* , i.e. c_i^* , $i = 1, \dots, 9$, from nine uniformly distributed points at A_j by tracking characteristics backward in time, i.e., solving the characteristics equations (2.4) starting from c_i , $i = 1 \dots, 9$, see the layout in Figure 2.3 (a).
- (1b) Construct a quadratic curve to approximate each side of the upstream cell. In particular, to construct the quadratic curve, $\widehat{c_1^*, c_2^*, c_3^*}$ as shown in Figure 2.3 (b), we perform the

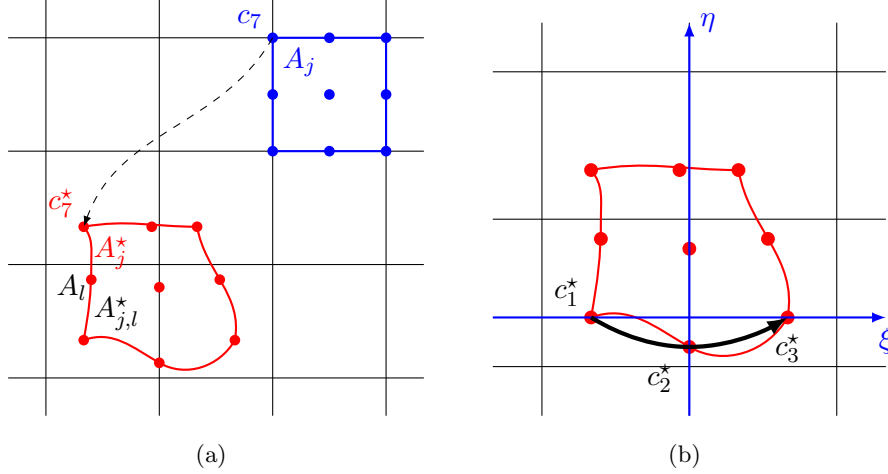


Figure 2.3: Schematic illustration of the SLDG formulation in two dimensions: quadratic-curved quadrilateral approximation to an upstream cell.

following procedure. First, we can construct a linear coordinate transformation $x - v$ to $\xi - \eta$ such that the coordinates of c_1^* and c_3^* are $(-1, 0)$ and $(1, 0)$ in $\xi - \eta$ space, respectively (see Figure 2.3 (b)). The coordinate transformation is given by

$$\begin{cases} x = \frac{x_3^* - x_1^*}{2} \xi + \frac{v_3^* - v_1^*}{2} \eta + \frac{x_3^* + x_1^*}{2}, \\ v = \frac{v_3^* - v_1^*}{2} \xi - \frac{x_3^* - x_1^*}{2} \eta + \frac{v_3^* + v_1^*}{2}. \end{cases} \quad (2.17)$$

By such a transformation, we can get the $\xi - \eta$ coordinate for the point c_2^* as (ξ_2, η_2) . Based on the date point $(-1, 0)$, (ξ_2, η_2) and $(1, 0)$, we construct the quadratic curve as follows

$$\widehat{c_1^*, c_2^*, c_3^*} : \eta(x, v) = \frac{\eta_2}{\xi_2^2 - 1} (\xi(x, v)^2 - 1). \quad (2.18)$$

(3) Search algorithm of outer line segments. We compute all the intersections between grid lines and four curved-sides of the upstream cell A_j^* and organize them in the counterclockwise order for outer line segments \mathcal{L}_q , $q = 1, \dots, N_o$. Specifically, to find intersection points between grid lines and $\widehat{c_1^*, c_2^*, c_3^*}$, we solve the following equations

$$\begin{cases} x_i = \frac{x_3^* - x_1^*}{2} \xi + \frac{v_3^* - v_1^*}{2} \eta + \frac{x_3^* + x_1^*}{2} \text{ (intersection with grid line } x = x_i), \\ \eta = \frac{\eta_2}{\xi_2^2 - 1} (\xi^2 - 1) \end{cases} \quad (2.19)$$

and

$$\begin{cases} v_j = \frac{v_3^* - v_1^*}{2} \xi - \frac{x_3^* - x_1^*}{2} \eta + \frac{v_3^* + v_1^*}{2} \text{ (intersection with grid line } v = v_j), \\ \eta = \frac{\eta_2}{\xi_2^2 - 1} (\xi^2 - 1). \end{cases} \quad (2.20)$$

Using the algorithm provided in Appendix A to solve (2.19)-(2.20), we can obtain all intersection points.

(4) **Evaluation of line integrals along outer line segments.** The integral along outer line segments $\sum_{q=1}^{N_o} \int_{\mathcal{L}_q} [Pdx + Qdv]$ can be evaluated by the following parameterization for each line segment. Assume that \mathcal{L}_q is part of the side $\widehat{c_1^*, c_2^*, c_3^*}$. Substituting (2.18) into (2.17), we

have

$$\begin{cases} x(\xi) = \frac{x_3^* - x_1^*}{2} \xi + \frac{v_3^* - v_1^*}{2} \frac{\eta_2}{\xi_2^2 - 1} (\xi^2 - 1) + \frac{x_3^* + x_1^*}{2}, \\ v(\xi) = \frac{v_3^* - v_1^*}{2} \xi - \frac{x_3^* - x_1^*}{2} \frac{\eta_2}{\xi_2^2 - 1} (\xi^2 - 1) + \frac{v_3^* + v_1^*}{2}. \end{cases} \quad (2.21)$$

Hence,

$$\int_{\mathcal{L}_q} [Pdx + Qdv] = \int_{\xi^{(q)}}^{\xi^{(q+1)}} [P(x(\xi, \eta), v(\xi, \eta))x'(\xi) + Q((\xi, \eta), v(\xi, \eta))v'(\xi)] d\xi, \quad (2.22)$$

where $(\xi^{(q)}, \eta^{(q)})$ and $(\xi^{(q+1)}, \eta^{(q+1)})$ are the start and end points of \mathcal{L}_q in $\xi - \eta$ coordinate, respectively. The integrand in (2.22) is a polynomial and thus the integral can be exactly computed by a numerical quadrature rule with sufficient degree of precision.

2.5 Positivity-preserving limiter

If the initial condition for the VP system (1.1) is positive, then the solution always stays positive as time evolves. Such a property is called positivity preservation. In our SLDG schemes, it can be shown that the updated cell averages at t^{n+1} stay positive, if the numerical solution f^n at t^n is positive. Similar to [31, 22, 23], in order to preserve positivity of numerical solutions, we further apply a high order positivity-preserving (PP) limiter [38] into the proposed SLDG scheme, which can be implemented as follows. The numerical solution $f(x, v, t^n)$ in cell A_j is modified by $\tilde{f}(x, v)$

$$\tilde{f}(x, v) = \theta(f(x, v, t^n) - \bar{f}) + \bar{f}, \quad \theta = \min \left\{ \left| \frac{\bar{f}}{m' - \bar{f}} \right|, 1 \right\},$$

where \bar{f} is the cell average of the numerical solution and m' is the minimum value of $f(x, v, t^n)$ over A_j . For P^1 polynomials, the minimum value can be found by comparing the values at four vertices of A_j . For P^2 polynomials, besides the four vertices, all critical points inside A_j should be considered to determine the function's minimum value. Note that the proposed SLDG schemes with the PP limiter feature the L^1 conservation property and hence the L^1 stability for nonnegative initial conditions. The proof follows a similar argument in [31].

2.6 The efficient implementation

In this subsection, we propose an efficient implementation of the P^2 SLDG method with quadratic-curved upstream cells using the third order temporal scheme (2.9)-(2.10). As shown in Section 2.2, for updating the numerical solution from t^n to t^{n+1} , this third order scheme includes two prediction steps (2.6), (2.8), and one correction step (2.13). To save some computational cost, we propose to use lower order SLDG schemes in two predictions steps. The efficient implementation of the P^2 SLDG method with quadratic-curved upstream cells using the third order scheme is summarized in the flow chart named as **Algorithm 1** below. Note that the efficient implementation will not compromise that accuracy of the scheme, which can be verified by a simple Taylor expansion. The numerical results presented in the next section also justifies the efficiency of the economical implementation.

Algorithm 1: The P^2 SLDG method with quadratic-curved upstream cells using the third order scheme:

1. The first order prediction:

- Solve the electric field E by the LDG method, based on the solution f^n .
- Trace the characteristics (2.4) for a time step Δt by the first order scheme (2.5).
- Evolve the solution f^n by using P^0 SLDG (i.e. only the cell averages are used and updated) with the quadrilateral approximation to upstream cells to get $f^{n+1,(1)}$.

2. The second order prediction:

- Solve the electric field E by the LDG method, based on the solution $f^{n+1,(1)}$.
- Trace the characteristics (2.4) for a time step Δt by the second order scheme (2.7).
- Evolve the solution $f^{n+1,(1)}$ by using P^1 SLDG with the quadrilateral approximation to upstream cells to get $f^{n+1,(2)}$.

3. The third order correction:

- Solve the electric field E by the LDG method, based on the solution $f^{n+1,(2)}$.
- Trace the characteristics (2.4) for a time step Δt by the second order scheme (2.9)-(2.10).
- Evolve the solution $f^{n+1,(2)}$ by using P^2 SLDG with quadratic-curved quadrilateral approximation to upstream cells to get f^{n+1} .

3 Numerical Results

In this section, for the VP system, we examine the performance of the proposed SLDG method with second/third order temporal accuracy, denoted by P^k SLDG-time2/3, with quadrilateral or quadratic-curved (QC) quadrilateral approximation to upstream cells (using the notation without or with QC). We implement the regular as well as efficient versions of the numerical scheme as described in Section 2.6 (using the notation without or with E). In all of our numerical tests, we let the time step size $\Delta t = \frac{CFL}{\frac{v_{\max}}{\Delta x} + \frac{\max(|E|)}{\Delta v}}$, where CFL is specified for different runs. For example, P^2 SLDG-QC-time3-E-CFL10 refers to the efficient implementation of the SLDG scheme with P^2 solution space, with quadratic-curved quadrilateral approximation to upstream cells, using third order scheme in characteristics tracing and with $CFL = 10$. We apply PP limiter for all test examples. We also note that the proposed SLDG methods are stable and highly accurate under very large CFL numbers as shown in numerical tests in this section. However, if an excessively large CFL number is used, some approximated upstream cells may become distorted, leading to a breakdown of the scheme. When the distortion happens in the simulation, a smaller time step should be used so that no distortion appears.

In this section, we demonstrate the following different aspects via extensive numerical tests of the proposed algorithm on a set of benchmark VP examples.

1. *Using a high order characteristics tracing scheme.* For weak Landau damping, we benchmark the numerical damping rate of the electrostatic field E against the theoretical value from the linear theory. In particular, we test the SLDG method with second and third order characteristics tracing schemes using CFL numbers as large as 20. In Figure 3.4, we showed the advantage of using a third order characteristics tracing scheme (compared with a second order one) for its superior performance in capturing the correct damping rate with CFL as large as 20.
2. *Spatial order of convergence: the need to use quadratic curves in approximating sides of upstream cells.* We test the spatial order of convergence in Table 3.1 for strong Landau damping, and in Table 3.4 for two stream instabilities. The computational effort in using a quadratic-curved quadrilateral approximation of upstream cells is justified by smaller error magnitudes observed and the corresponding third order convergence for the SLDG scheme

with P^2 polynomial space.

3. *Temporal order of convergence.* We test the temporal order of convergence in Table 3.2 for strong Landau damping and in Table 3.5 and 3.6 for two stream instabilities. Simulations with large $CFLs$, ranging from 5 to 50 or more, provide decent results.
4. *CPU savings for the efficient implementation of the SLDG scheme.* We compare the numerical performance and CPU time for the “regular” and “efficient” implementation of the SLDG scheme in Table 3.1 and 3.4. In particular, for the P^2 SLDG scheme, more than 30% savings in CPU time are observed, while the accuracy is not compromised. Due to similar performance and significant savings in CPU time, most of our tests are done base on the efficient implementation.
5. *CPU comparison between the SLDG scheme and the classical RKDG.* We perform CPU comparison between the SLDG and RKDG methods in Tables 3.2 and 3.5. Per time step evolution, an SLDG scheme takes about four times as much CPU time as that of a RKDG counterpart with the same order accuracy. On the other hand, for stability of an Eulerian RKDG method, the upper bound of the CFL is about $\frac{1}{2k+1}$, with k being the polynomial degree; while for an SLDG scheme, the CFL number can be taken as large as 50, leading to tremendous savings in CPU time (50% to 90% savings). We can choose the time stepping size purely for accuracy consideration, without much constraint from stability.
6. *Preservation of mass and other physical norms.* In the VP system, the following physical quantities should remain constant in time. Tracking relative deviations of these quantities numerically provides a good measurement of the quality of numerical schemes. Our proposed SLDG scheme is locally and globally mass conservative. We will show comparable (sometimes superior) performance in preserving the physical norms for the proposed SLDG scheme with large $CFLs$.

1. Mass:

$$\text{Mass} = \int_v \int_x f(x, v, t) dx dv.$$

2. L^p norm, $1 \leq p < \infty$:

$$\|f\|_p = \left(\int_v \int_x |f(x, v, t)|^p dx dv \right)^{\frac{1}{p}}.$$

3. Energy:

$$\text{Energy} = \int_v \int_x f(x, v, t) v^2 dx dv + \int_x E^2(x, t) dx,$$

where $E(x, t)$ is the electric field.

4. Entropy:

$$\text{Entropy} = \int_v \int_x f(x, v, t) \log(f(x, v, t)) dx dv.$$

Example 3.1. (*Weak Landau damping.*) Consider weak Landau damping for the VP system. The initial condition is set to be the following perturbed equilibrium

$$f(x, v, t = 0) = \frac{1}{\sqrt{2\pi}} (1 + \alpha \cos(kx)) \exp\left(-\frac{v^2}{2}\right), \quad (3.1)$$

with $\alpha = 0.01$ and $k = 0.5$. Our computational domain is $[0, 4\pi] \times [-v_{\max}, v_{\max}]$. We truncate the velocity domain at $v_{\max} = 2\pi$. This test case has been numerically investigated by several authors (e.g. see [20, 28, 33, 25, 24, 21, 5, 29]).

In Figure 3.4, we present the time evolution of L^2 norm of the electric field (in semi-log scale) for P^2 SLDG-time2-E and P^2 SLDG-time3-E schemes using a mesh of 128×128 elements and different CFL s. As expected, the decay rate from simulations with $CFL = 1$ matches well with the theoretical value $\gamma = -0.1533$ [20] (the solid line in the same plots). For $CFL = 10$, both results match well with the theoretical value; for $CFL = 20$, the third order characteristics tracing scheme exhibits superior performance, compared with the second order one, in capturing the correct damping rate in the long run.

Example 3.2. (*Strong Landau damping.*) Consider strong Landau damping for the VP system. The initial condition is the same as weak one (3.1), but with a larger perturbation parameter $\alpha = 0.5$. The computational domain is $[0, 4\pi] \times [-2\pi, 2\pi]$.

In Table 3.1, we test the spatial convergence of the proposed SLDG scheme with the third order characteristic tracing scheme. We set $CFL = 0.1$ to minimize the error from time discretization. The well-known time reversibility of the VP system is used to test the order of convergence. In particular, one can integrate the VP system forward to some time T , and then reverse the velocity field of the solution and continue to integrate the system by the same amount of time T . Then, the solution should recover the initial condition with reverse velocity field, which can be used as a reference solution. We show the L^2 and L^∞ errors and the corresponding orders of convergence for P^k

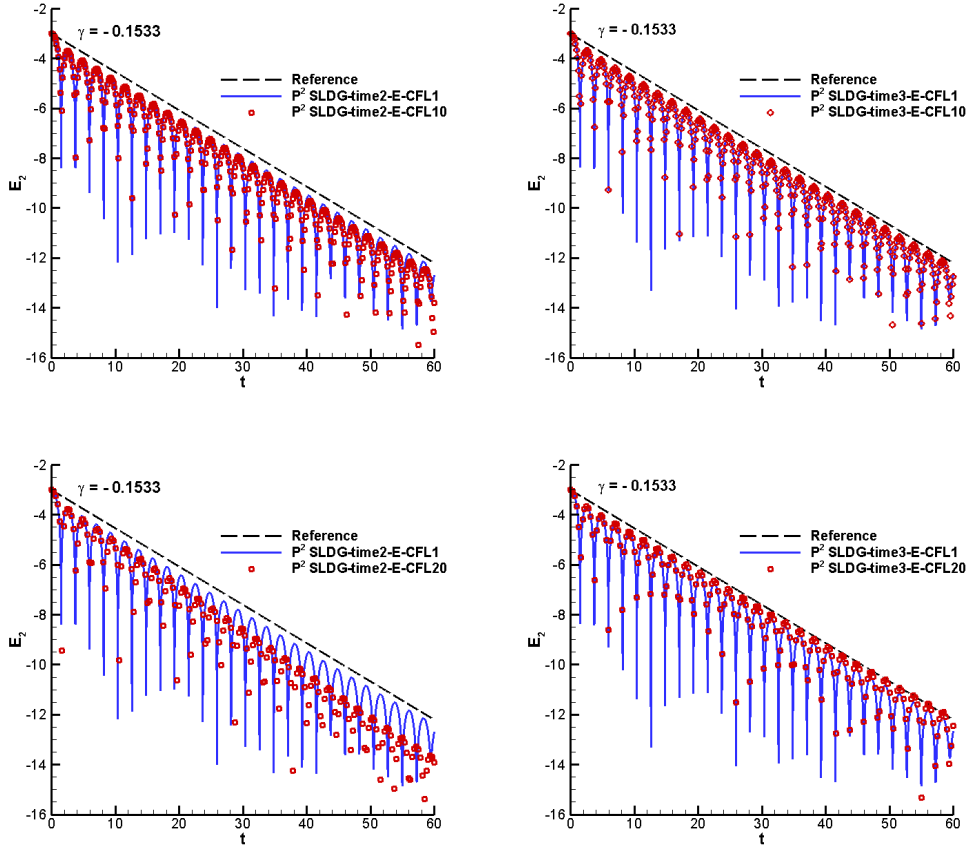


Figure 3.4: Weak Landau damping. Time evolution of electric field in L^2 norm. Solid line: $CFL = 1$. Square: $CFL = 10$ or $CFL = 20$. The 'Reference' line (dashed line) corresponds to the exponential decay in the amplitude of the oscillation ($\gamma = -0.1533$).

SLDG-(QC)-time3-(E) schemes with $CFL = 0.1$ in Table 3.1. Second order convergence is observed for P^1 SLDG scheme as expected. Second order convergence, with smaller error magnitudes than those for P^1 SLDG scheme, is observed for P^2 SLDG scheme with quadrilateral approximation to upstream cells. Such second order convergence is due to the use of straight lines in approximating sides of upstream cells, even though P^2 approximation space is employed. More importantly, if quadratic curves are used in approximating sides of upstream cells, the error is further reduced and the order of convergence is improved to third order, see the results for P^2 SLDG-QC scheme. 30% – 40% savings in CPU time are observed for the *efficient* implementation of P^2 SLDG schemes when compare with the CPU time needed for the *regular* implementation, while the accuracy is not compromised.

Second, temporal convergence from the characteristics tracing scheme used in the proposed

SLDG method is tested. Table 3.2 summarizes the L^2 and L^∞ errors and the corresponding temporal convergence rates for the P^k SLDG methods with the second and third order characteristic tracing schemes, where the time reversibility property of the VP system is used to compute the error. To make the temporal error dominant, we use a spatial mesh of 160×160 elements. In Table 3.2, around second and third order temporal accuracy is observed, for P^1 SLDG-time2-E and P^2 SLDG-QC-time3-E schemes, respectively, with $CFLs$ ranging from 5 to 25. Also in Table 3.2, we perform CPU time comparison between SLDG and RKDG schemes. Per time step, the SLDG scheme costs about 4 times as much CPU time as that of the classical RKDG method. On the other hand, the SLDG scheme allows for a much larger CFL . For example, if $CFL = 25$, then time stepping size of the SLDG scheme is 125 times as large as that for a RKDG scheme, leading to tremendous savings in CPU time. Note that, the RKDG code, that we use for CPU comparison, has been optimized for its CPU efficiency.

We show the time evolution of the electric field in the L^2 norm (in semi-log scale) in Figure 3.5. The linear decay rate γ_1 (measured as the slope of a line originating from the local maximum of the second peak to the third peak), as well as the growth rate γ_2 (measured as the slope of a line originating from the local maximum of the tenth peak to the sixteenth peak) are summarized in Table 3.3, and they agree with the results reported in the literature [20, 33, 25, 24]. Furthermore, in Figure 3.6, we plot time evolutions of the relative derivation of the discrete L^1 norm, L^2 norm, energy and entropy. In particular, we observe that (1) The error for the L^1 norm (on the order of 10^{-9}) is due to the truncation of the velocity domain, which can be further reduced by using a larger velocity domain in simulations; (2) In general, the P^2 SLDG method does a better job in conserving these physical norms than the P^1 SLDG method; (3) Compared to the SLDG schemes with larger $CFLs$, the schemes with smaller $CFLs$ are able to better conserve the energy, but perform worse in conserving the L^2 norm and entropy. (4) The SLDG methods outperform the RKDG method in conserving energy. In Figure 3.7, we present the contour plots of the solutions at $T = 40$ computed by the P^2 SLDG-QC-time3-E scheme method and the P^2 RKDG method with the mesh of 160×160 elements. We observe that the SLDG scheme with $CFL = 10$ and the RKDG scheme with $CFL = 0.2$ generate very consistent numerical results. Meanwhile, the SLDG method with $CFL = 30$ is still stable and able to generate decent results: the main structures of the solution are captured, but some mild wiggles are observed.

Table 3.1: Strong Landau damping with $T = 0.5$. Order of accuracy in space and CPU time for P^k SLDG-(QC)-time3-(E) scheme. We set $CFL = 0.1$ so that the spatial error is the dominant error.

Mesh	L^2 error	Order	L^∞ error	Order	CPU	L^2 error	Order	L^∞ error	Order	CPU
P^1 SLDG-time3						P^1 SLDG-time3-E				
32^2	1.21E-3		1.18E-2		2.28	1.21E-3		1.18E-2		2.17
64^2	3.15E-4	1.94	3.49E-3	1.76	17.51	3.15E-4	1.94	3.49E-3	1.76	16.09
96^2	1.42E-4	1.97	1.61E-3	1.91	58.50	1.42E-4	1.97	1.61E-3	1.91	55.10
128^2	8.02E-5	1.98	9.18E-4	1.95	139.60	8.02E-5	1.98	9.18E-4	1.95	129.78
160^2	5.15E-5	1.99	5.92E-4	1.97	275.96	5.15E-5	1.99	5.92E-4	1.97	252.92
P^2 SLDG-time3						P^2 SLDG-time3-E				
32^2	2.18E-4		1.97E-3		4.96	2.18E-4		1.95E-3		3.12
64^2	5.57E-5	1.97	5.03E-4	1.97	37.50	5.57E-5	1.97	4.72E-4	2.04	24.68
96^2	2.50E-5	1.98	2.25E-4	1.99	126.96	2.50E-5	1.98	2.11E-4	1.99	81.09
128^2	1.41E-5	1.98	1.27E-4	2.00	315.18	1.41E-5	1.98	1.19E-4	2.00	201.04
160^2	9.07E-6	1.99	8.10E-5	2.00	602.12	9.07E-6	1.99	7.60E-5	2.00	391.17
P^2 SLDG-QC-time3						P^2 SLDG-QC-time3-E				
32^2	8.32E-5		1.08E-3		5.29	8.32E-5		1.08E-3		3.59
64^2	1.02E-5	3.03	1.38E-4	2.97	41.50	1.02E-5	3.03	1.36E-4	2.98	27.60
96^2	3.00E-6	3.02	4.08E-5	3.00	141.18	3.00E-6	3.02	4.02E-5	3.01	91.87
128^2	1.26E-6	3.01	1.71E-5	3.03	334.73	1.26E-6	3.01	1.68E-5	3.02	221.90
160^2	6.43E-7	3.01	8.58E-6	3.08	645.90	6.43E-7	3.01	8.45E-6	3.09	433.79

Table 3.2: Strong Landau damping with $T = 0.5$, and with the mesh of 160×160 . Temporal order of convergence and CPU comparison between SLDG and RKDG schemes.

CFL	L^2 error	Order	L^∞ error	Order	CPU (sec)
P^1 SLDG-time2-E					
0.3	5.05E-05	–	5.90E-04	–	47.79
5	3.97E-05	–	5.67E-04	–	3.23
10	4.67E-05	0.23	6.27E-04	0.15	1.67
15	1.04E-04	1.97	1.04E-03	1.24	1.32
20	1.96E-04	2.21	1.44E-03	1.14	1.01
25	3.91E-04	3.08	2.45E-03	2.37	0.71
P^1 RKDG					
0.3	4.36E-05	–	4.17E-04	–	5.26
P^2 SLDG-QC-time3-E					
0.2	6.37E-07	–	8.43E-06	–	229.92
5	2.35E-06	–	1.30E-05	–	9.50
10	1.69E-05	2.85	9.87E-05	2.92	5.14
15	6.15E-05	3.19	2.83E-04	2.60	3.89
20	1.32E-04	2.65	5.97E-04	2.60	2.98
25	2.43E-04	2.74	1.11E-03	2.79	2.01
P^2 RKDG					
0.2	8.68E-07	–	1.09E-05	–	41.39

Example 3.3. (*Two Stream instability I.*) Consider two stream instability, with an unstable initial

Table 3.3: Strong Landau damping. $T = 0.5$. A mesh of 160×160 is used. The linear decay rate γ_1 and the growth rate γ_2 .

CFL	γ_1		γ_2	
	P^1 SLDG-time2-E		P^2 SLDG-QC-time3-E	
1	-0.2907	0.0847	-0.2907	0.0868
10	-0.2875	0.0848	-0.2842	0.0866
20	-0.3054	0.0840	-0.3125	0.0867

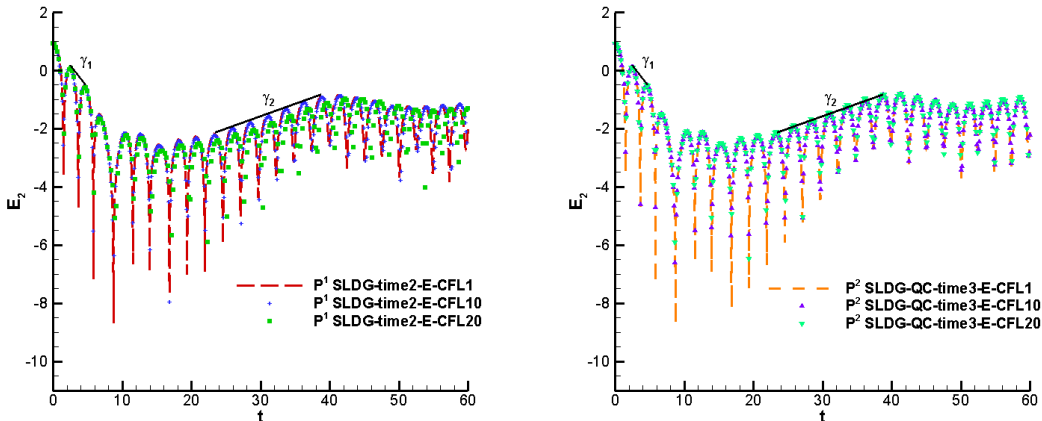


Figure 3.5: Strong Landau damping: The SLDG schemes are equipped with the PP limiter. Time evolution of the electric field in L^2 .

distribution function,

$$f(x, v, t = 0) = \frac{2}{7\sqrt{2\pi}}(1 + 5v^2)(1 + \alpha((\cos(2kx) + \cos(3kx))/1.2 + \cos(kx))) \exp\left(-\frac{v^2}{2}\right)$$

with $\alpha = 0.01$, $k = 0.5$ on the computation domain $[0, 4\pi] \times [-10, 10]$.

We first present the spatial convergence of the SLDG schemes in Table 3.4. As in the previous example, we make use of the time reversibility of VP system to test the order of convergence. Slightly less than second order accuracy is observed for the P^1 SLDG-time2-E scheme. The error magnitude of the P^2 SLDG-time3-E scheme is much smaller than the corresponding one of the P^1 SLDG-time2-E scheme, while order reduction is still observed due to the fact that we use straight lines to approximate sides of upstream cells. When quadratic curves are used to approximate sides of upstream cells, the errors are further reduced and around third order convergence is observed for the P^2 SLDG-QC scheme. Similar to strong Landau damping, 30% – 40% savings in CPU time are observed for P^2 SLDG-(QC)-time3 schemes with *efficient* implementation.

We test the temporal convergence of the SLDG schemes for this example. In order to make the

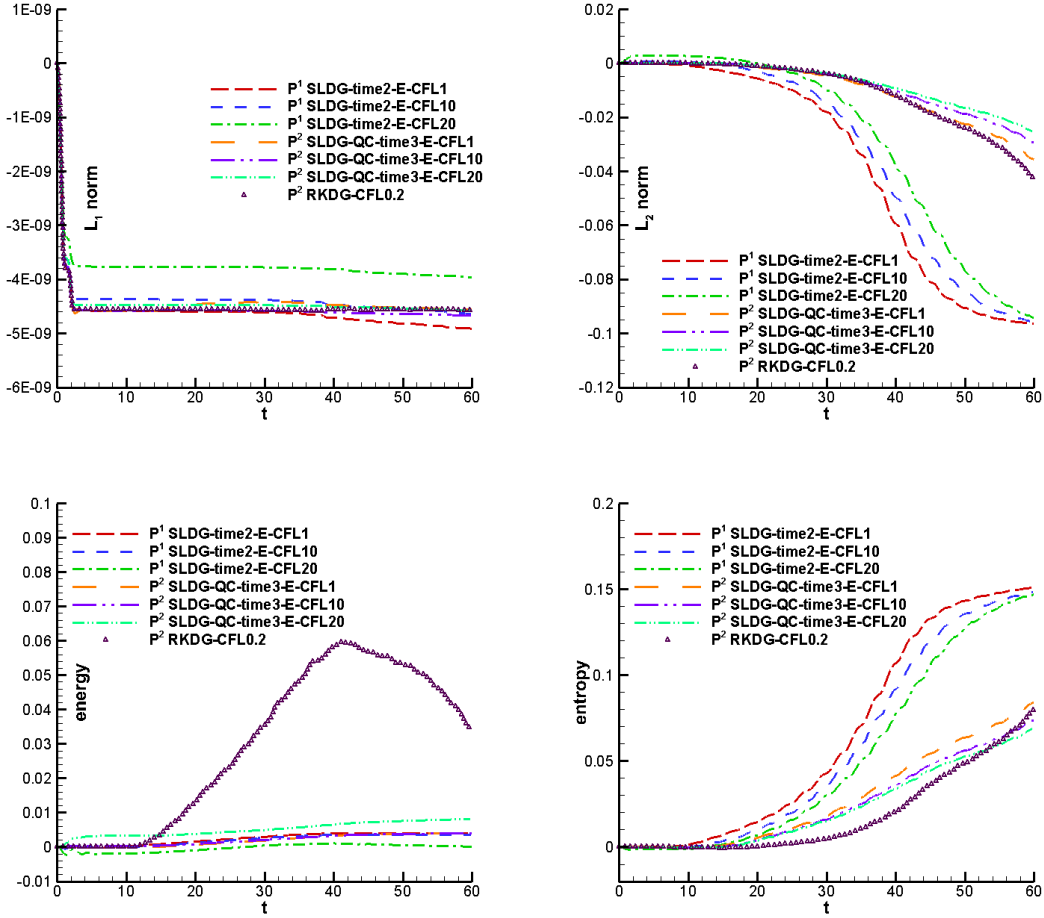
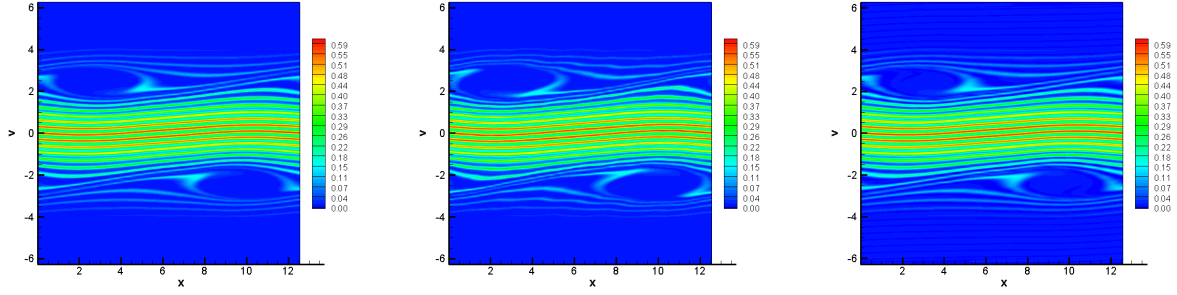


Figure 3.6: Strong Landau damping. Time evolution of the relative deviations of L^1 (upper left) and L^2 (upper right) norms of the solution as well as the discrete kinetic energy (lower left) and entropy (lower right).

temporal error dominant, we use a spatial mesh of 160×160 elements. The convergence results, as well as CPU comparison with RKDG methods, are presented in Table 3.5. For this example, even from the accuracy point of view, CFL for the P^1 SLDG scheme can be taken to be as large as 50 (compared with 0.3 for a P^1 RKDG scheme) with comparable performance in terms of magnitude of errors. Again, the corresponding savings in CPU time are tremendous compared with RKDG methods: it takes 7.35 seconds for the RKDG method to reach the final integration time $T = 0.5$; while it takes less than one second for the SLDG method. Similar comments apply to the comparison of CPU time between the P^2 SLDG and RKDG schemes. Table 3.5 demonstrates the superior performance and efficiency of the proposed SLDG method. In order to show the temporal convergence rate of the SLDG scheme, we present Table 3.6, where the reference solution comes



(a) P^2 SLDG-QC-time3-E with $CFL = 10$ (b) P^2 SLDG-QC-time3-E with $CFL = 30$ (c) P^2 RKDG with $CFL = 0.2$

Figure 3.7: Strong Landau damping with the spatial mesh of 160×160 . $T = 40$. (a): P^2 SLDG-QC-time3-E with $CFL = 10$. (b): P^2 SLDG-QC-time3-E with $CFL = 30$. (c): P^2 RKDG with $CFL = 0.2$.

from the simulation with the same spatial mesh but with relatively small $CFL = 0.1$. Expected second and third order convergence rates are observed.

Lastly, we show time evolution of the electric field in the L^2 norm (in semi-log scale) for the P^1 SLDG-time2-E and P^2 SLDG-QC-time3-E schemes using a mesh of 160×160 elements and different CFL s in Figure 3.8. In Figure 3.9, we show the relative derivation of the discrete L^1 norm, L^2 norm, energy and entropy. We observe that all methods are able to conserve the L^1 norm up to the truncation error from the velocity domain. The ability of SLDG methods to conserve these physical norms is satisfactory and comparable to the RKDG method. In Figure 3.10, we plot the numerical solutions of phase space profiles at $T = 40$. We observe that the solutions computed by the P^2 SLDG-QC-time3-E scheme with $CFL = 10, 30$ are consistent with that by the P^2 RKDG scheme with $CFL = 0.2$.

Example 3.4. (*Two Stream instability II.*) Consider the symmetric two stream instability [35, 17], with the perturbed equilibrium as the initial condition

$$f(x, v, t = 0) = \frac{1}{2v_t\sqrt{2\pi}} \left[\exp\left(-\frac{(v-u)^2}{2v_{th}^2}\right) + \exp\left(-\frac{(v+u)^2}{2v_{th}^2}\right) \right] (1 + 0.05 \cos(kx)).$$

where $u = 0.99$, $k = \frac{2}{13}$, and $v_t = 0.3$. We let $v_{\max} = 2\pi$ and use a spatial mesh of 160×160 elements. We plot the time evolution of the electric field in the L^2 and L^∞ norms (in semi-log scale) in Figure 3.11, which is benchmarked against the results reported in the literature. Time evolution of the relative derivation of the discrete L^1 norm, L^2 norm, energy and entropy in Figure 3.12.

Table 3.4: Two Stream instability I at $T = 0.5$. Spatial order of accuracy and CPU time for the SLDG method. We set $CFL = 0.1$ so that the spatial error is the dominant error.

Mesh	L^2 error	Order	L^∞ error	Order	CPU	L^2 error	Order	L^∞ error	Order	CPU
P^1 SLDG-time3						P^1 SLDG-time3-E				
32^2	4.28E-3		2.28E-2		3.17	4.28E-3		2.28E-2		2.93
64^2	1.10E-3	1.97	7.29E-3	1.65	24.89	1.10E-3	1.97	7.29E-3	1.65	23.04
96^2	4.91E-4	1.98	3.60E-3	1.74	83.18	4.91E-4	1.98	3.60E-3	1.74	75.06
128^2	2.79E-4	1.96	2.21E-3	1.69	194.60	2.79E-4	1.96	2.21E-3	1.69	182.12
160^2	1.81E-4	1.93	1.53E-3	1.65	395.15	1.81E-4	1.93	1.53E-3	1.65	354.96
P^2 SLDG-time3						P^2 SLDG-time3-E				
32^2	5.33E-4		2.80E-3		6.78	5.33E-4		2.79E-3		4.35
64^2	7.47E-5	2.84	3.88E-4	2.85	53.62	7.47E-5	2.84	3.87E-4	2.85	34.25
96^2	2.52E-5	2.67	1.63E-4	2.14	179.95	2.52E-5	2.68	1.63E-4	2.14	113.35
128^2	1.30E-5	2.31	1.20E-4	1.08	419.73	1.30E-5	2.31	1.19E-4	1.08	270.32
160^2	8.61E-6	1.84	1.00E-4	0.80	821.60	8.60E-6	1.84	9.99E-5	0.80	520.23
P^2 SLDG-QC-time3						P^2 SLDG-QC-time3-E				
32^2	5.34E-4		2.81E-3		7.45	5.34E-4		2.81E-3		4.92
64^2	7.41E-5	2.85	3.72E-4	2.92	58.42	7.41E-5	2.85	3.72E-4	2.92	38.93
96^2	2.39E-5	2.79	1.28E-4	2.63	202.46	2.39E-5	2.79	1.28E-4	2.63	131.04
128^2	1.08E-5	2.76	6.03E-5	2.62	469.59	1.08E-5	2.76	6.03E-5	2.62	312.01
160^2	5.87E-6	2.74	3.29E-5	2.72	891.53	5.87E-6	2.74	3.29E-5	2.72	596.71

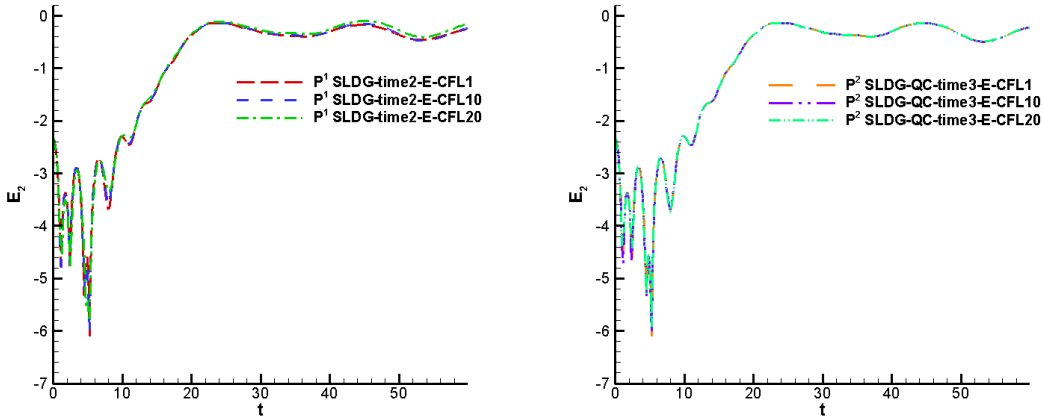


Figure 3.8: Two-stream instability I. Time evolution of the electric field in L^2 .

Figure 3.13 shows the numerical solutions of phase space profiles computed by the P^2 SLDG-QC-time3-E method with $CFL = 10, 15$ and the P^2 RKDG method with $CFL = 0.2$ at $T = 40$. Decent numerical performance of the P^2 SLDG-QC-time3-E method with $CFL = 10$ and the P^2 RKDG method with $CFL = 0.2$ is observed. On the other hand, the P^2 SLDG-QC-time3-E method with a large $CFL = 15$ is still stable and generates reasonable result, but some mild wiggles are observed. Note that, for this example, distortion of approximate upstream cells (hence the break down of the

Table 3.5: Two Stream instability I at $T = 0.5$. A mesh of 160×160 is used. Temporal order of convergence for the SLDG method via the time reversibility of the VP system.

CFL	L^2 error	Order	L^∞ error	Order	CPU
P^1 SLDG-time2-E					
0.3	1.81E-04	–	1.53E-03	–	64.65
45	2.07E-04	–	1.56E-03	–	0.70
50	2.31E-04	1.05	1.63E-03	0.42	0.70
55	2.73E-04	1.76	1.91E-03	1.65	0.70
60	3.42E-04	2.60	2.36E-03	2.46	0.70
65	4.21E-04	2.58	2.87E-03	2.42	0.39
P^1 RKDG					
0.3	1.83E-04	–	1.51E-03	–	7.35
P^2 SLDG-QC-time3-E					
0.2	5.87E-06	–	3.29E-05	–	307.57
5	5.85E-06	–	3.25E-05	–	12.31
10	5.96E-06	0.03	3.30E-05	0.02	6.75
15	7.23E-06	0.48	4.31E-05	0.66	4.81
20	1.18E-05	1.69	7.70E-05	2.01	3.93
25	1.89E-05	2.13	1.23E-04	2.11	3.00
30	3.52E-05	3.40	2.32E-04	3.46	2.98
35	4.72E-05	1.91	3.17E-04	2.03	2.01
40	6.49E-05	2.38	4.23E-04	2.16	2.00
45	9.75E-05	3.45	6.16E-04	3.19	1.97
50	1.46E-04	3.82	9.28E-04	3.90	1.92
P^2 RKDG					
0.2	6.98E-06	–	3.43E-05	–	57.29

Table 3.6: Two Stream instability I at $T = 0.5$. A mesh of 160×160 is used. Temporal order of convergence for the SLDG method.

CFL	L^2 error	Order	L^∞ error	Order
P^1 SLDG-time2-E				
5	3.16E-06	–	3.01E-05	–
10	8.83E-06	1.48	5.06E-05	0.75
15	1.94E-05	1.95	9.47E-05	1.55
20	3.52E-05	2.06	1.64E-04	1.91
25	5.03E-05	1.60	2.30E-04	1.52
P^2 SLDG-QC-time3-E				
5	1.26E-07	–	1.23E-06	–
10	6.60E-07	2.39	5.59E-06	2.18
15	2.20E-06	2.97	1.54E-05	2.50
20	5.26E-06	3.03	3.69E-05	3.04
25	9.61E-06	2.70	6.69E-05	2.67

code) is observed for the P^2 SLDG-QC-time3-E method with $CFL = 20$.

Example 3.5. (*Bump-on-tail instability.*) Consider an unstable bump-on-tail problem [1, 36] with the initial distribution as

$$f(x, v, t = 0) = f_{BOT}(v)(1 + 0.04 \cos(kx)).$$

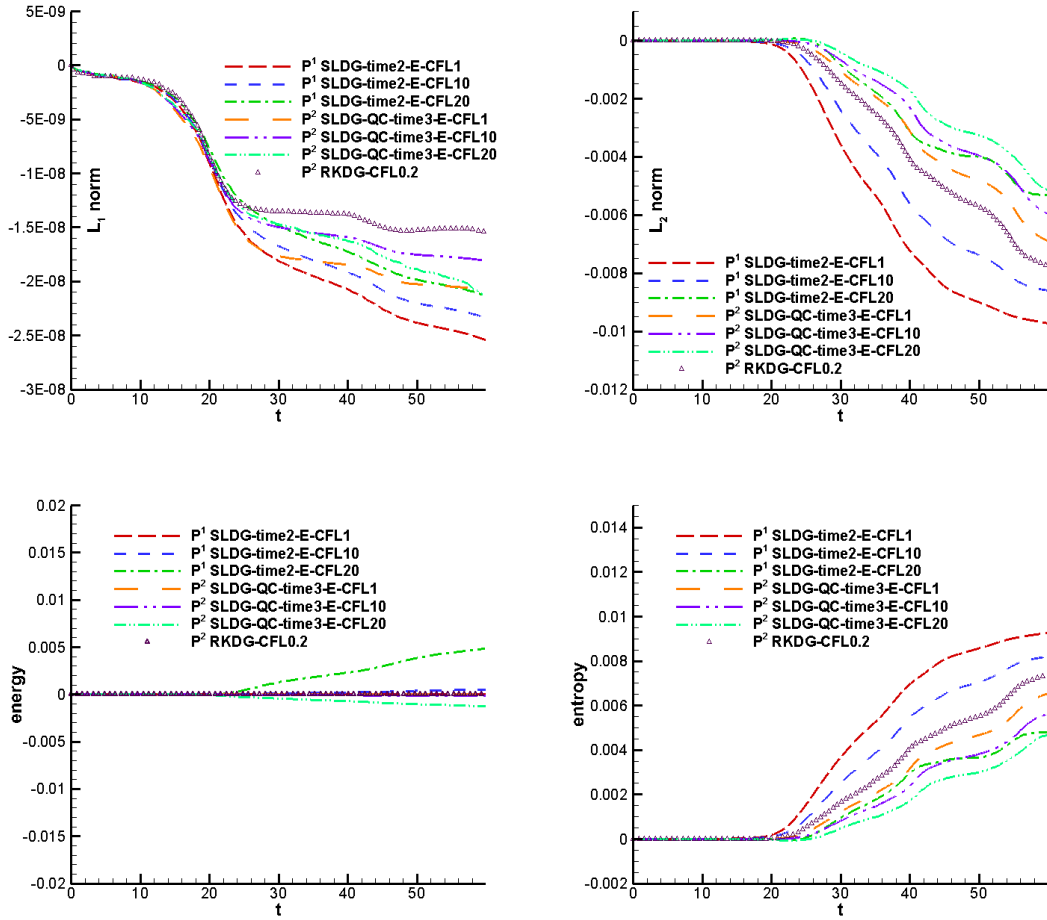


Figure 3.9: Two-stream instability I. Time evolution of L^1 (upper left) and L^2 (upper right) norms of the solution as well as the discrete kinetic energy (lower left) and entropy (lower right).

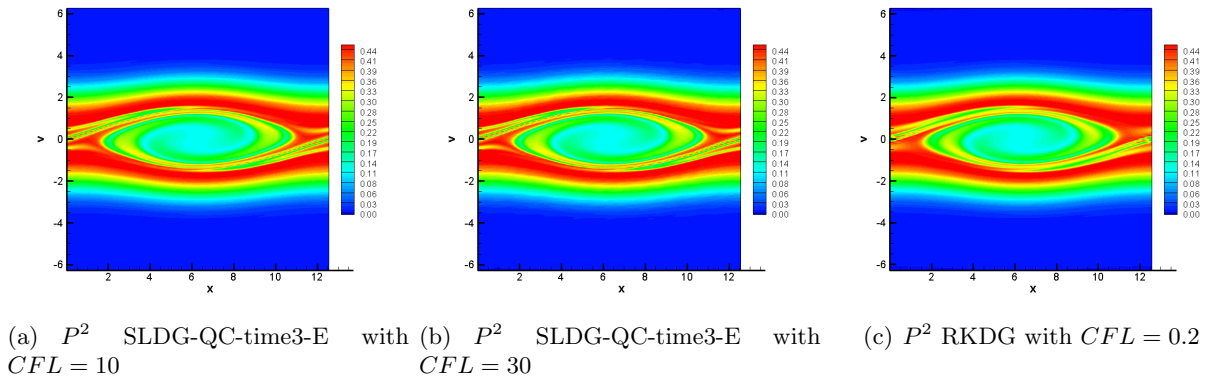


Figure 3.10: Two stream instability I at $T = 40$. Mesh: 160×160 . (a): P^2 SLDG-QC-time3-E with $CFL = 10$. (b): P^2 SLDG-QC-time3-E with $CFL = 30$. (c): P^2 RKDG with $CFL = 0.2$.

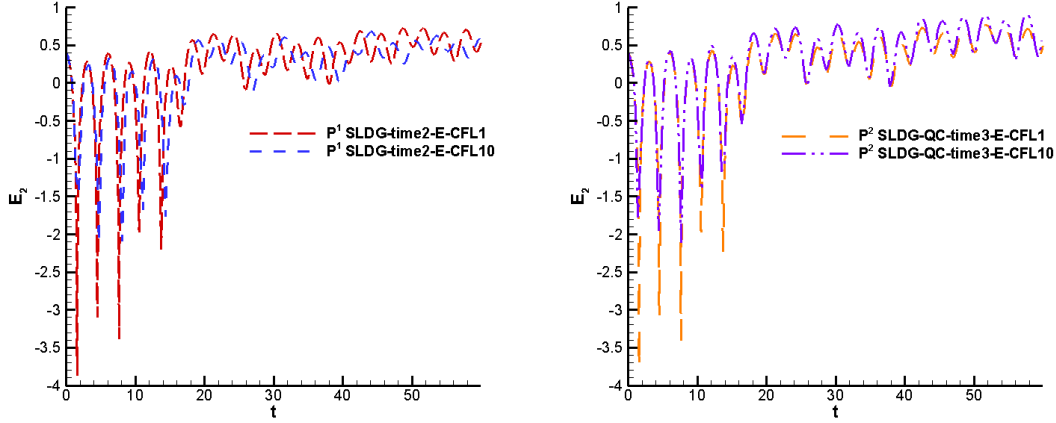


Figure 3.11: Two stream instability II. Time evolution of the electric field in L^2 .

where the bump-on-tail distribution is

$$f_{BOT}(v) = n_p \exp\left(-\frac{v^2}{2}\right) + n_b \exp\left(-\frac{(v-u)^2}{2v_t^2}\right),$$

The parameters are chosen to be $n_p = \frac{9}{10\sqrt{2\pi}}$, $n_b = \frac{2}{10\sqrt{2\pi}}$, $u = 4.5$, $v_t = 0.5$, $k = 0.3$. The computational domain is $[0, \frac{20}{3}\pi] \times [-13, 13]$. We show the time evolution of the electric field in L^2 norm (in semi-log scale) in Figure 3.14, and show the time evolution of the relative derivation of the discrete L^1 norm, L^2 norm, energy and entropy in Figure 3.15. In Figure 3.16, we plot the numerical solutions of phase space profiles computed by the P^2 SLDG-QC-time3-E method with $CFL = 10, 30$ and the P^2 RKDG method with $CFL = 0.2$ at $T = 40$. As in Example 3.3, the proposed SLDG schemes with CFL as large as 30 are still able to generate very consistent results with that by the P^2 RKDG method with $CFL = 0.2$, leading to great computational savings.

4 Conclusion

A high order SLDG method was proposed for solving the VP system. The two key ingredients of the proposed scheme are (1) a high order non-splitting conservative SLDG transport scheme and (2) a high order characteristics tracking approach for the VP system. The proposed method is locally mass conservative, highly accurate, free of splitting error and allows for extra large time stepping size. To the best of the authors' knowledge, this is the first SLDG scheme that is able to attain all these desired properties. The numerical performance of the method is promising. We compare the CPU time of an efficient implementation of the proposed method, with that of

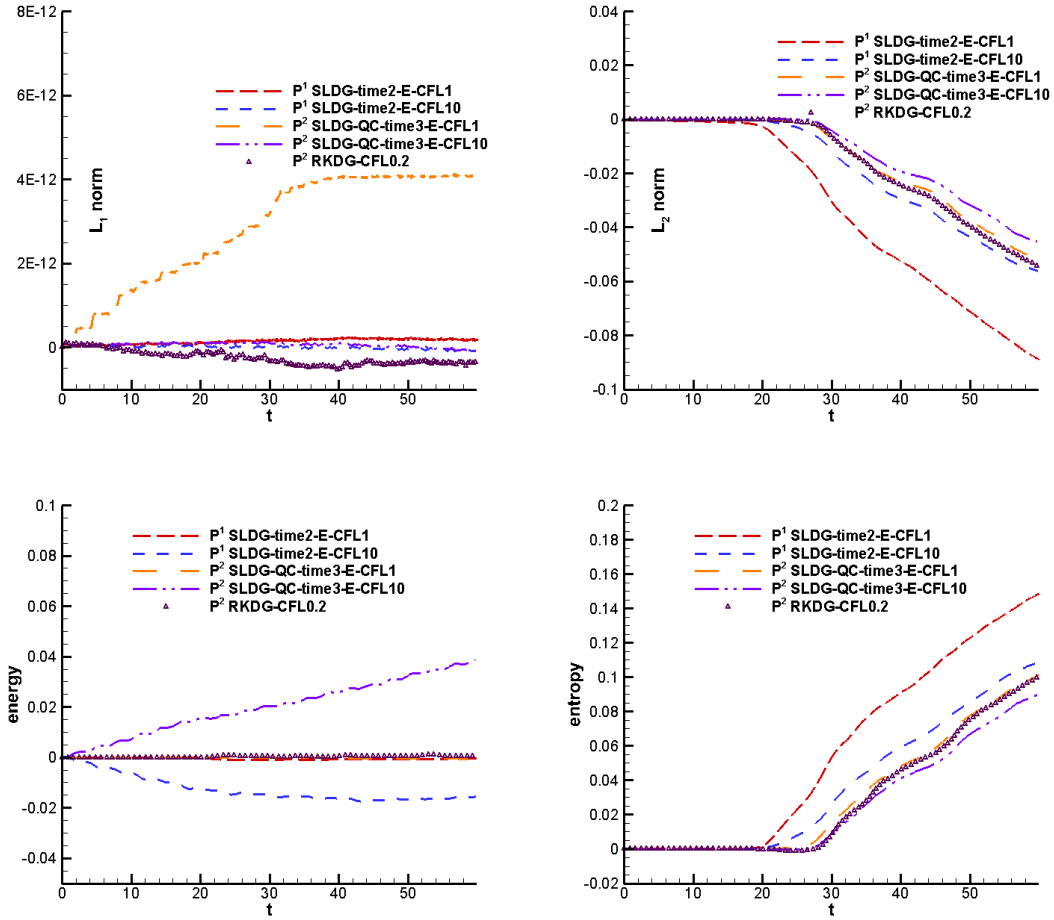


Figure 3.12: Two stream instability II. Time evolution of L^1 (upper left) and L^2 (upper right) norms of the solution as well as the discrete kinetic energy (lower left) and entropy (lower right).

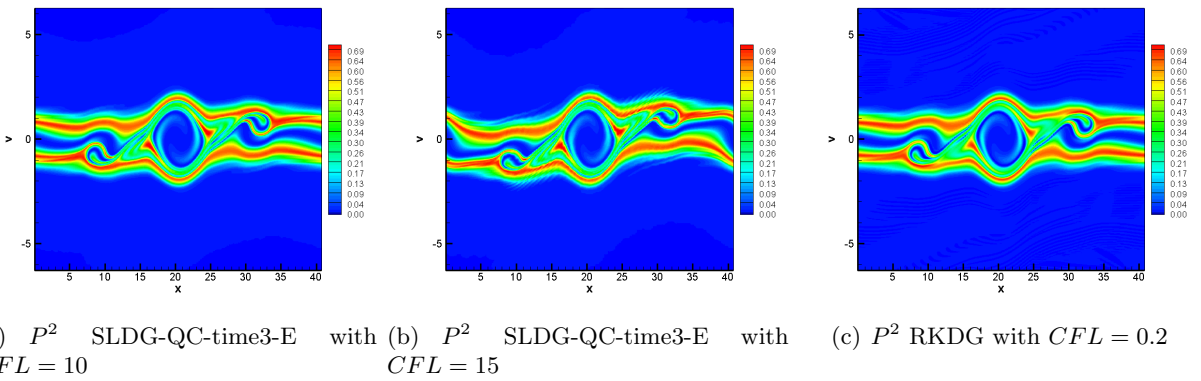


Figure 3.13: Two stream instability II at $T = 40$. Mesh: 160×160 . (a): P^2 SLDG-QC-time3-E with $CFL = 10$. (b): P^2 SLDG-QC-time3-E with $CFL = 15$. (c): P^2 RKDG with $CFL = 0.2$.

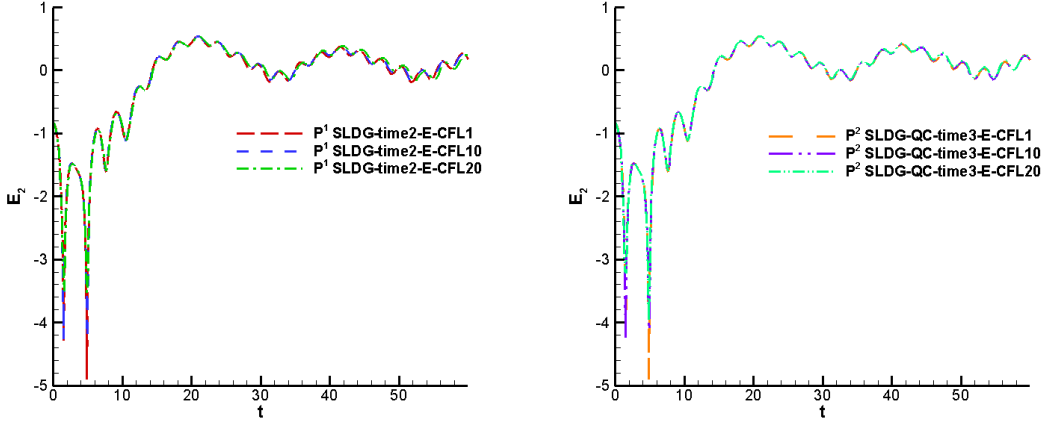


Figure 3.14: Bump-on-tail instability. Time evolution of the electric field in L^2 .

the Eulerian RK DG method, in many benchmark VP test problems. Tremendous computational savings are observed, without compromising effectiveness of the method. We will perform rigorous error estimate, investigate superconvergence properties, and generalize the scheme to handle non-trivial boundary conditions, diffusion terms, source terms, etc. in our future work. The extension to the VP system in higher dimensions will be explored as well.

A Search intersection points between quadratic-curved sides of an upstream cell and background grid lines

The algorithm for searching intersection points between an upstream cell and the grid line $x = x_i$ is described in the following. The procedure for searching intersection points between the upstream cell and $v = v_j$ is pretty similar, thus omitted for brevity. We can find intersection points of the quadratic curve determined by points (x_1^*, v_1^*) , (x_2^*, v_2^*) , (x_3^*, v_3^*) and grid line $x = x_i$ by solving the following equation,

$$\begin{cases} x_i = \frac{x_3^* - x_1^*}{2} \xi + \frac{v_3^* - v_1^*}{2} \eta + \frac{x_3^* + x_1^*}{2}, \\ \eta = \frac{\eta_2}{\xi_2^2 - 1} (\xi^2 - 1). \end{cases} \quad (\text{A.1})$$

Case 1 If $|x_3^* - x_1^*| \leq |v_3^* - v_1^*|$, we have the following equation derived from (A.1),

$$A\xi^2 + B\xi + C = 0. \quad (\text{A.2})$$

where

$$A = \frac{\eta_2}{\xi_2^2 - 1}, \quad B = \frac{x_3^* - x_1^*}{v_3^* - v_1^*}, \quad C = -\frac{\left(x_i - \frac{x_1^* + x_3^*}{2}\right)}{\frac{v_3^* - v_1^*}{2}} - \frac{\eta_2}{\xi_2^2 - 1}.$$

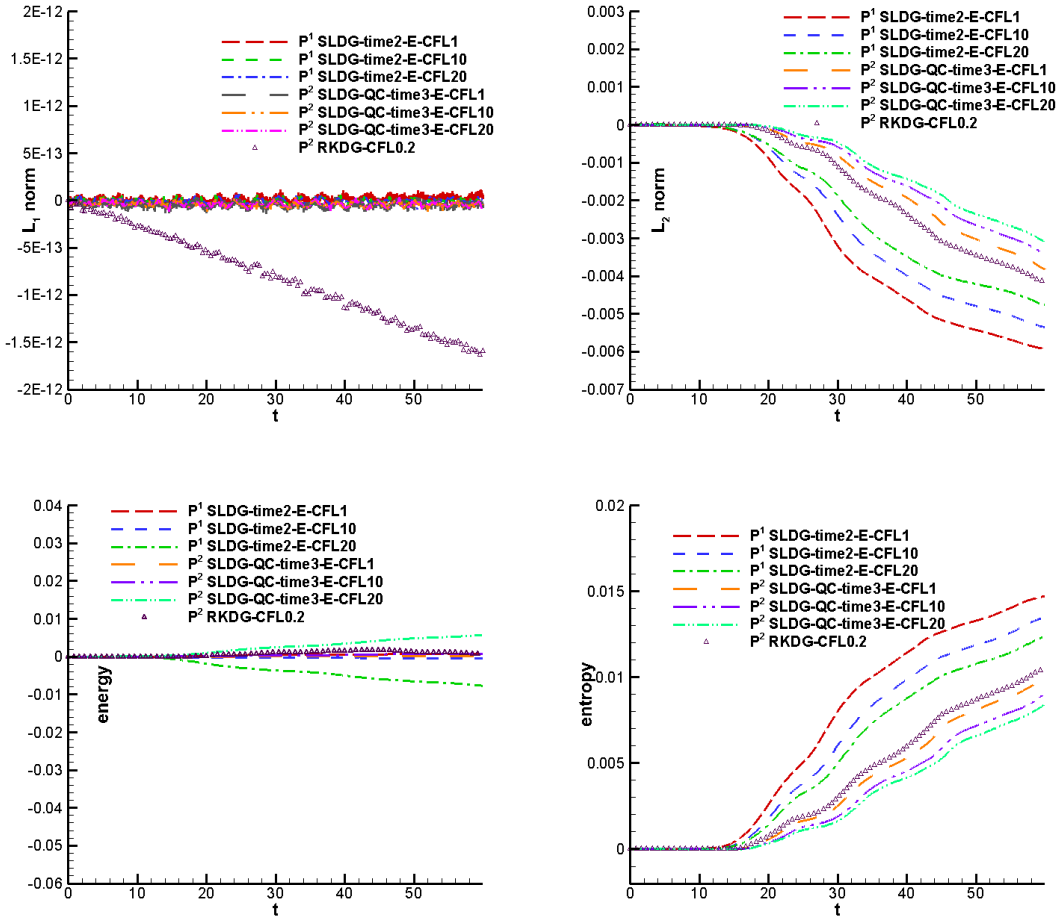


Figure 3.15: Bump-on-tail instability. Time evolution of L^1 (upper left) and L^2 (upper right) norms of the solution as well as the discrete kinetic energy (lower left) and entropy (lower right).

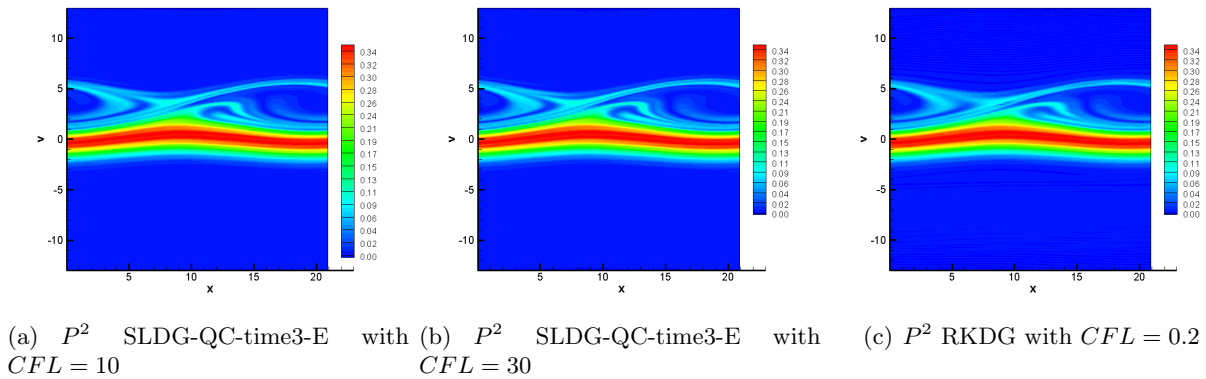


Figure 3.16: Bump-on-tail instability. Mesh: 160×160 . (a): P^2 SLDG-QC-time3-E with $CFL = 10$. (b): P^2 SLDG-QC-time3-E with $CFL = 30$. (c): P^2 RKDG with $CFL = 0.2$.

We can solve (A.2) as follows:

if $A \geq \varepsilon$, where $\varepsilon = 10^{-13}$ **then**

Let $\Delta = B^2 - 4AC$.

If $\Delta < 0$, there is no solution.

If $\Delta = 0$, there is only one solution, $\xi_1 = -\frac{B}{2A}$.

If $\Delta > 0$, there are two solutions,

$$\xi_1 = \frac{2C}{-B - \gamma\sqrt{\Delta}}, \quad \xi_2 = \frac{-B - \gamma\sqrt{\Delta}}{2A},$$

where $\gamma = 1$ if $B \geq 0$, and $\gamma = -1$ otherwise.

else if $A < \varepsilon$ and $B \geq \varepsilon$ **then**

there is only one solution, $\xi_1 = -\frac{C}{B}$.

else

We retreat this case as no intersection points.

end if

If $\xi \in [-1, 1]$, the solution (ξ, η) is identified as an intersection point.

Case 2 If $|x_3^* - x_1^*| > |v_3^* - v_1^*|$, we have the following equation derived from (A.1),

$$A\eta^2 + B\eta + C = 0,$$

where

$$\begin{aligned} A &= \frac{\eta_2}{\xi_2^2 - 1} \left(\frac{v_3^* - v_1^*}{x_3^* - x_1^*} \right)^2, \\ B &= -1 - \frac{4 \left(x_i - \frac{x_1^* + x_3^*}{2} \right) v_3^* - v_1^*}{x_2^* - x_1^*} \frac{\eta_2}{x_3^* - x_1^* \xi_2^2 - 1}, \\ C &= \frac{\eta_2}{\xi_2^2 - 1} \left(\frac{4 \left(x_i - \frac{x_1^* + x_3^*}{2} \right)^2}{(x_3^* - x_1^*)^2} - 1 \right). \end{aligned}$$

Similar to Case 1.1, the solution η can be solved. And then,

$$\xi = \frac{2x_i - x_3^* - x_1^*}{x_3^* - x_1^*} - \frac{v_3^* - v_1^*}{x_3^* - x_1^*} \eta. \quad (\text{A.3})$$

If $\xi \in [-1, 1]$, the solution (ξ, η) is identified as an intersection point.

References

- [1] T. Arber and R. Vann. A critical comparison of Eulerian-grid-based Vlasov solvers. *Journal of computational physics*, 180(1):339–357, 2002.

- [2] D. Arnold, F. Brezzi, B. Cockburn, and L. Marini. Unified analysis of discontinuous Galerkin methods for elliptic problems. *SIAM Journal on Numerical Analysis*, 39(5):1749–1779, 2002.
- [3] C. Birdsall and A. Langdon. *Plasma physics via computer simulation*. CRC Press, 2005.
- [4] X. Cai, W. Guo, and J.-M. Qiu. A high order conservative semi-Lagrangian discontinuous Galerkin method for two-dimensional transport simulations. *Journal of Scientific Computing*, accepted, 2017.
- [5] X. Cai, J. Qiu, and J.-M. Qiu. A conservative semi-Lagrangian HWENO method for the Vlasov equation. *Journal of Computational Physics*, 323:95–114, 2016.
- [6] J. Carrillo and F. Vecil. Nonoscillatory interpolation methods applied to Vlasov-based models. *SIAM Journal on Scientific Computing*, 29(3):1179–1206, 2007.
- [7] F. Casas, N. Crouseilles, E. Faou, and M. Mehrenberger. High-order Hamiltonian splitting for the Vlasov–Poisson equations. *Numerische Mathematik*, 135(3):769–801, 2017.
- [8] P. Castillo, B. Cockburn, I. Perugia, and D. Schötzau. An a priori error analysis of the local discontinuous Galerkin method for elliptic problems. *SIAM Journal on Numerical Analysis*, 38(5):1676–1706, 2000.
- [9] C. Cheng and G. Knorr. The integration of the Vlasov equation in configuration space. *Journal of Computational Physics*, 22(3):330–351, 1976.
- [10] Y. Cheng, A. Christlieb, and X. Zhong. Energy-conserving discontinuous Galerkin methods for the Vlasov–Ampère system. *Journal of Computational Physics*, 256:630–655, 2014.
- [11] Y. Cheng, A. Christlieb, and X. Zhong. Energy-conserving discontinuous Galerkin methods for the Vlasov–Maxwell system. *Journal of Computational Physics*, 279:145–173, 2014.
- [12] Y. Cheng, I. Gamba, F. Li, and P. Morrison. Discontinuous Galerkin methods for the Vlasov–Maxwell equations. *SIAM Journal on Numerical Analysis*, 52(2):1017–1049, 2014.
- [13] Y. Cheng, I. Gamba, and P. Morrison. Study of conservation and recurrence of Runge–Kutta discontinuous Galerkin schemes for Vlasov–Poisson systems. *Journal of Scientific Computing*, 56(2):319–349, 2013.

- [14] A. Christlieb, W. Guo, M. Morton, and J.-M. Qiu. A high order time splitting method based on integral deferred correction for semi-Lagrangian Vlasov simulations. *Journal of Computational Physics*, 267:7–27, 2014.
- [15] B. Cockburn, G. Karniadakis, and C.-W. Shu. *Discontinuous Galerkin Methods, Theory, Computation and Applications*. DOE/ER/25372-Final, Brown University, Providence, RI (US), 2000.
- [16] B. Cockburn and C.-W. Shu. The local discontinuous Galerkin method for time-dependent convection-diffusion systems. *SIAM Journal on Numerical Analysis*, 35(6):2440–2463, 1998.
- [17] N. Crouseilles, M. Mehrenberger, and E. Sonnendrücker. Conservative semi-Lagrangian schemes for Vlasov equations. *Journal of Computational Physics*, 229(6):1927–1953, 2010.
- [18] F. Filbet and E. Sonnendrücker. Comparison of Eulerian Vlasov solvers. *Computer Physics Communications*, 150(3):247–266, 2003.
- [19] F. Filbet, E. Sonnendrücker, and P. Bertrand. Conservative numerical schemes for the Vlasov equation. *Journal of Computational Physics*, 172(1):166–187, 2001.
- [20] F. Filbet, E. Sonnendrücker, and P. Bertrand. Conservative numerical schemes for the Vlasov equation. *Journal of Computational Physics*, 172(1):166–187, 2001.
- [21] Y. Güçlü, A. J. Christlieb, and W. N. Hitchon. Arbitrarily high order Convected Scheme solution of the Vlasov–Poisson system. *Journal of Computational Physics*, 270:711–752, 2014.
- [22] W. Guo, R. Nair, and J.-M. Qiu. A conservative semi-Lagrangian discontinuous Galerkin scheme on the cubed-sphere. *Monthly Weather Review*, 142(1):457–475, 2013.
- [23] W. Guo, R. Nair, and X. Zhong. An efficient WENO limiter for discontinuous Galerkin transport scheme on the cubed sphere. *International Journal for Numerical Methods in Fluids*, 81:3–21, 2015.
- [24] W. Guo and J.-M. Qiu. Hybrid semi-Lagrangian finite element-finite difference methods for the Vlasov equation. *Journal of Computational Physics*, 234:108–132, 2013.

- [25] R. Heath, I. Gamba, P. Morrison, and C. Michler. A discontinuous Galerkin method for the Vlasov–Poisson system. *Journal of Computational Physics*, 231(4):1140–1174, 2012.
- [26] P. Lauritzen, R. Nair, and P. Ullrich. A conservative semi-Lagrangian multi-tracer transport scheme (CSLAM) on the cubed-sphere grid. *Journal of Computational Physics*, 229(5):1401–1424, 2010.
- [27] T. Nakamura and T. Yabe. Cubic interpolated propagation scheme for solving the hyper-dimensional Vlasov–Poisson equation in phase space. *Computer Physics Communications*, 120(2):122–154, 1999.
- [28] J.-M. Qiu and A. Christlieb. A Conservative high order semi-Lagrangian WENO method for the Vlasov Equation. *Journal of Computational Physics*, 229:1130–1149, 2010.
- [29] J.-M. Qiu and G. Russo. A High Order Multi-Dimensional Characteristic Tracing Strategy for the Vlasov–Poisson System. *Journal of Scientific Computing*, 71(1):414–434, 2017.
- [30] J.-M. Qiu and C.-W. Shu. Conservative semi-Lagrangian finite difference WENO formulations with applications to the Vlasov equation. *Communications in Computational Physics*, 10(4):979, 2011.
- [31] J.-M. Qiu and C.-W. Shu. Positivity preserving semi-Lagrangian discontinuous Galerkin formulation: Theoretical analysis and application to the Vlasov–Poisson system. *Journal of Computational Physics*, 230(23):8386–8409, 2011.
- [32] M. Restelli, L. Bonaventura, and R. Sacco. A semi-Lagrangian discontinuous Galerkin method for scalar advection by incompressible flows. *Journal of Computational Physics*, 216(1):195–215, 2006.
- [33] J. A. Rossmannith and D. C. Seal. A positivity-preserving high-order semi-Lagrangian discontinuous Galerkin scheme for the Vlasov–Poisson equations. *Journal of Computational Physics*, 230(16):6203–6232, 2011.
- [34] E. Sonnendruecker, J. Roche, P. Bertrand, and A. Ghizzo. The semi-Lagrangian method for the numerical resolution of the Vlasov equation. *Journal of Computational Physics*, 149(2):201–220, 1999.

- [35] T. Umeda. A conservative and non-oscillatory scheme for Vlasov code simulations. *Earth, planets and space*, 60(7):773–779, 2008.
- [36] T. Xiong, J.-M. Qiu, Z. Xu, and A. Christlieb. High order maximum principle preserving semi-Lagrangian finite difference WENO schemes for the Vlasov equation. *Journal of Computational Physics*, 273:618–639, 2014.
- [37] T. Xiong, G. Russo, and J.-M. Qiu. Conservative multi-dimensional semi-Lagrangian finite difference scheme: stability and applications to the kinetic and fluid simulations. *arXiv preprint arXiv:1607.07409*, 2016.
- [38] X. Zhang and C.-W. Shu. On maximum-principle-satisfying high order schemes for scalar conservation laws. *Journal of Computational Physics*, 229:3091–3120, 2010.